J. of KOSOMBE
Vol. 19, No. 2, 133-141, 1998

Quantitative Analysis of Bayesian SPECT Reconstruction : Effects of Using Higher-Order Gibbs Priors

S.J. Lee

Department of Electronic Engineering, Cornma Paichai University

(Received November 26, 1997, Accepted April 2, 1998)

요 약 : Bayesian SPECT 영상재구성에 있어서 정교한 형태의 사전정보를 사용할 경우 bias 및 variance와 같은 통계적 차원에서의 정량적 성능을 향상시킬 수 있다. 특히, "thin plate"와 같은 高次의 smoothing 사전정보는 "membrane"과 같은 일반적인 다른 사전정보에 비해 bias를 개선시키는 것으로 알려져 있다. 그러나, 이와 같은 장점은 영상재구성 알고리즘에 내재하는 hyperparameters의 값을 최적으로 선택하였을 경우에만 적용된다. 본 연구에서는 thin plate와 membrane의 두 가지 대표적인 사전정보를 포함하는 영상재구성 알고리즘의 정량적 성능에 대해 집중 고찰한다. 즉, 알고리즘에 내재하는 hyperparameters가 통계적 차원에서 bias와 variance에 어떠한 영향을 미치는지 관찰한다. 실험에서 Monte Carlo noise trials를 사용하여 bias와 variance를 계산하며, 각 결과를 ML-EM 및 filtered backprojection으로부터 얻어진 bias 및 variance 와 비교한다. 결론적으로 thin plate와 같은 高次 의 사전정보는 hyperparameters의 선택에 민감하지 않으며, hyperparameters 값의 전 범위에 걸쳐 bias를 개선시킴을 보인다.

Abstract : In Bayesian SPECT reconstruction, the incorporation of elaborate forms of priors can lead to improved quantitative performance in various statistical terms, such as bias and variance. In particular, the use of higher-order smoothing priors, such as the thin-plate prior, is known to exhibit improved bias behavior compared to the conventional smoothing priors such as the membrane prior. However, the bias advantage of the higher-order priors is effective only when the hyperparameters involved in the reconstruction algorithm are properly chosen. In this work, we further investigate the quantitative performance of the two representative smoothing priors - the thin plate and the membrane - by observing the behavior of the associated hyperparameters of the prior distributions. In our experiments we use Monte Carlo noise trials to calculate bias and variance of reconstruction estimates, and compare the performance of ML-EM estimates to that of regularized EM using both membrane and thin-plate priors, and also to that of filtered backprojection, where the membrane and thin plate models become simple apodizing filters of specified form. We finally show that the use of higher-order models yields excellent "robustness" in quantitative performance by demonstrating that the thin plate leads to very low bias error over a large range of hyperparameters, while keeping a reasonable variance.

Key words : Bayesian reconstruction, Gibbs distribution, Quantitation, Hyperparameter

INTRODUCTION

In single-photon emission computed tomography (SPECT), the radiopharmaceutical, designed to show physiological function of a particular organ in the body, is injected into the patient and localizes within one or more organs based on its biochemical properties. The objective of SPECT is to determine the three-dimensional (3-D) distribution of radionuclide concentrations within the body using 2-D projectional views acquired at many different angles about the patient. Since SPECT systems, in practice, inherently involve noise and several physical factors that degrade the projection data, the quality of image reconstructions is poor when the measurements are assumed to be made with infinite accuracy. Over the last decade, a variety of statistical reconstruction methods[1-7] have been introduced and have enjoyed continuing interest since they can in principle overcome the above problems associated with the classical deterministic reconstruction methods, such as filtered backprojection (FBP). The well-known ML-EM (maximum-likelihood expectation-maximization) approach for reconstruction is attractive in that it can naturally express accurate system

통신저자 : 이수진, (302-735) 대전시 서구 도마 2동 439-6 배재대학교 전자공학과
Tel. (042)520-5711, Fax. (042)520-5663
E-mail : sjlee@woonam.paichai.ac.kr

models of physical effects, and can accurately model the statistical character of the data. However, it is known to be unstable for the noise levels and numbers of measurements that characterize SPECT. In contrast, regularized EM in the context of a Bayesian maximum *a posteriori* (MAP) framework overcomes this instability by incorporating prior information while retaining the above advantages of ML-EM approaches. Priors in a Bayesian approach are probabilistic descriptions of the spatial character of the underlying emission object. Since it is difficult to infer global properties of the underlying source, most common approaches involve assumptions on the *local* spatial characteristics of the underlying source and model the prior probability as Gibbs distributions which are equivalent to Markov random fields (MRFs). In these approaches, neighboring pixels in the underlying source are assumed to have similar intensities.

In recent years, many Gibbs priors have been proposed in the literature; some of these implicitly model the underlying radionuclide density as globally smooth[6,8], and others extend the smoothness model by allowing for spatial discontinuities[2,4,7,9,10]. Discontinuity preservation is associated with a smoothing penalty that is a nonquadratic function[7] of nearby pixel differences, whereas conventional (e.g. membrane) smoothing priors use quadratic penalties. Although these priors can exhibit good performance, their applications to the clinic is hindered mainly by the difficulty in the choice of hyperparameters that control the degree of regularity in the reconstruction. Several methods to estimate values of hyperparameters have been proposed[11-13]. However, most of the methods are computationally expensive and far from routine applications. Therefore, a reconstruction algorithm that involves hyperparameters may be more practical if it can exhibit a good performance even in the case of imperfect selection of hyperparameters. This is related to the "robustness" of a reconstruction algorithm with respect to hyperparameters involved in the algorithm.

In our previous work[14], we showed that a new quadratic smoothing prior for SPECT reconstruction, the thin plate (TP), offers good performance compared to the membrane (MM) prior in that, unlike the priors with first derivatives, the TP prior recovers graded (ramplike or soft-edged) source characteristic of realistic distributions more effectively without incurring large bias errors due to the smoothing of edge regions. In this work, we further investigate the advantages of TP priors in terms of various quantitations. We evaluate and compare, by using Monte Carlo noise trials, the quantitative performance of the quadratic smoothing priors - the membrane and the thin plate. The behavior of the associated hyperparameters of the prior distributions is then observed and characterized in a systematic way. We finally show that the use of second-derivatives yields excellent robustness in both bias and variance by demonstrating that TP leads to very low bias error over a large range of smoothing parameter, while keeping a reasonable variance.

MAXIMUM *A POSTERIORI* APPROACHES

The MAP approach in the context of a Bayesian framework is to estimate the underlying source field $\boldsymbol{f}$ by maximizing the posterior probability, given as

$$\Pr(\boldsymbol{F}=\boldsymbol{f} \mid \boldsymbol{G}=\boldsymbol{g})=\frac{\Pr(\boldsymbol{G}=\boldsymbol{g} \mid \boldsymbol{F}=\boldsymbol{f})\Pr(\boldsymbol{F}=\boldsymbol{f})}{\Pr(\boldsymbol{G}=\boldsymbol{g})} \quad (1)$$

where $\boldsymbol{f}$ and $\boldsymbol{g}$ are 2-D vector fields for the source intensities and projection data, respectively, and $\boldsymbol{F}$ and $\boldsymbol{G}$ are the associated random fields. Given the posterior distribution in (1), maximizing the posterior distribution is equivalent to minimizing -log of the posterior probability and the MAP estimation reduces to

$$\hat{\boldsymbol{f}}=\arg\min_{\boldsymbol{f}}[-\log \Pr(\boldsymbol{G}=\boldsymbol{g} \mid \boldsymbol{F}=\boldsymbol{f})-\log \Pr(\boldsymbol{F}=\boldsymbol{f})],$$

where the two terms on the right side are the likelihood and the prior, respectively.

Since the number of detected counts in SPECT is independently Poisson distributed, we model the likelihood as :

$$\Pr(\boldsymbol{G}=\boldsymbol{g} \mid \boldsymbol{F}=\boldsymbol{f})=\prod_{t\theta}\frac{\bar{g}_{t\theta}^{\,g_{t\theta}}\exp(-\bar{g}_{t\theta})}{g_{t\theta}!} \quad (2)$$

where $\bar{g}_{t\theta}=\sum_{ij}H_{t\theta,ij}f_{ij}$. In (2) $g_{t\theta}$ is the number of detected counts in the detector bin indexed by t at angle θ, $\bar{g}_{t\theta}$ is the expected number of counts for a particular source $\boldsymbol{f}$, and $H_{t\theta,ij}$ is the probability that a photon emitted from source location (i,j) hits detector bin t at angle θ. The major physical factors for SPECT, attenuation, scatter, and detector response, can be adequately modeled as linear effects and summarized by the probability matrix $H_{t\theta,ij}$.

The likelihood energy then becomes

$$E_D(\boldsymbol{f}) = -\log \Pr(\boldsymbol{G}=\boldsymbol{g} \mid \boldsymbol{F}=\boldsymbol{f})$$
$$=\sum_{t\theta}[-g_{t\theta}\log(\bar{g}_{t\theta})] + \sum_{t\theta}\bar{g}_{t\theta},$$

where the term log $(g_{t\theta}!)$ was dropped since it does not involve $\boldsymbol{f}$.

To incorporate the MM and TP priors in a MAP approach, we model the prior probability as a Gibbs distribution given as

$$\Pr(\boldsymbol{F} = \boldsymbol{f}) = \frac{1}{Z}\exp[-\lambda E(\boldsymbol{f})],$$

where $\boldsymbol{f}$ is the 2-D source distribution comprising pixel components f_{ij}, E the associated Gibbs prior energy function, Z a normalization of no concern here, and λ the positive *hyperparameter* that weights the prior relative to the likelihood term. The function $E(\boldsymbol{f})$ is the weighted sum of energies of individual "cliques" which are defined by adjacent pixels in the neighborhood. The energy $E(\boldsymbol{f})$ for MM is given as

$$E_{MM}(\boldsymbol{f}) = \sum_{ij}\left[f_h^2(i,j) + f_v^2(i,j)\right]$$

for the four-nearest neighborhood system, and

$$E_{MM}(\boldsymbol{f}) = \sum_{ij}\left[f_h^2(i,j) + f_v^2(i,j) + \frac{1}{\sqrt{2}}f_d^2(i,j) + \frac{1}{\sqrt{2}}f_e^2(i,j)\right] \tag{3}$$

for the eight-nearest neighborhood system with discretizations of first partial derivatives given by

$$f_h(i,j) = f_{i,j+1} - f_{i,j},\quad f_v(i,j) = f_{i+1,j} - f_{i,j},$$
$$f_d(i,j) = f_{i-1,j+1} - f_{i,j},\quad f_e(i,j) = f_{i+1,j+1} - f_{i,j}.$$

For the thin plate, the energy is

$$E_{TP}(\boldsymbol{f}) = \sum_{ij}\left[f_{hh}^2(i,j) + f_{hv}^2(i,j) + f_{vv}^2(i,j)\right]. \tag{4}$$

Here, $f_{vv}(i,j)$ and $f_{hh}(i,j)$ denote the discrete second partial derivatives of the source distribution in the vertical and horizontal directions, respectively, and $f_{hv}(i,j)$ is the second partial cross derivative. Our choices for discretization of the derivatives are:

$$f_{hh}(i,j) = f_{i,j+1} - 2f_{i,j} + f_{i,j-1},$$
$$f_{vv}(i,j) = f_{i+1,j} - 2f_{i,j} + f_{i-1,j},$$
$$f_{hv}(i,j) = f_{i+1,j+1} - f_{i+1,j} - f_{i,j+1} + f_{i,j}.$$

In this work, we use (3) and (4) for MM and TP, respectively.

To find a minimum of the overall energy function that consists of the likelihood and the prior, we utilize the incomplete/complete data formulation of generalized EM-MAP (GEM-MAP) approach[2]. In this case the maximization step of the GEM-MAP algorithm results in the minimization of

$$E(\boldsymbol{f} \mid \hat{\boldsymbol{f}}^k) = -Q(\boldsymbol{f} \mid \hat{\boldsymbol{f}}^k) + \lambda E_p(\boldsymbol{f}),$$

where $\hat{\boldsymbol{f}}^k$ is the current (kth) estimate,

$$Q(\boldsymbol{f} \mid \hat{\boldsymbol{f}}^k) = \sum_{t\theta}\sum_{ij}\left[g_{t\theta}\frac{H_{t\theta,ij}\hat{f}_{ij}^k}{\sum_{m,n}H_{t\theta,mn}\hat{f}_{mn}^k}\log(f_{ij}) - H_{t\theta,ij}f_{ij}\right],$$

and $E_p(\boldsymbol{f})$ is the prior energy function given by either $E_{MM}(\boldsymbol{f})$ in (3) or $E_{TP}(\boldsymbol{f})$ in (4). To minimize the above M-step objective function, we use the method of Iterated Conditional Modes (ICM)[15]. ICM minimizes the energy function by a coordinate-wise descent procedure performed by minimizing the energy function with respect to f_{ij} while keeping all other source intensities fixed. After a full sweep of the lattice, the procedure is repeated until convergence criteria are met.

To find the solution that minimizes the M-step objective function, we set $\frac{\partial E(\boldsymbol{f} \mid \hat{\boldsymbol{f}})}{\partial f_{ij}} = 0$ and solve for f_{ij}. The ICM update equations for MM and TP are given by

$$\hat{f}_{ij}^{k+1} = \frac{-(\sum_{t\theta}H_{t\theta,ij} - 2\lambda X_3) + \sqrt{(\sum_{t\theta}H_{t\theta,ij} - 2\lambda X_3)^2 + 9\lambda X_2 X_1}}{4\lambda X_2},$$

where

$$X_1 = \sum_{t\theta}g_{t\theta}\frac{H_{t\theta,ij}\hat{f}_{ij}^k}{\sum_{t\theta}H_{t\theta,mn}\hat{f}_{mn}^k}$$

$$X_2 = 4 + 2\sqrt{2}$$

$$X_3 = \hat{f}_{i-1,j}^{k+1} + \hat{f}_{i,j-1}^{k+1} + \hat{f}_{i,j+1}^{k} + \hat{f}_{i+1,j}^{k} + \frac{\sqrt{2}}{2}(\hat{f}_{i-1,j-1}^{k+1} + \hat{f}_{i-1,j+1}^{k+1} + \hat{f}_{i+1,j-1}^{k} + \hat{f}_{i+1,j+1}^{k})$$

for MM, and

$$X_2 = 20,$$

$$X_3 = 8(\hat{f}_{i-1,j}^{k+1} + \hat{f}_{i,j-1}^{k+1} + \hat{f}_{i,j+1}^{k} + \hat{f}_{i+1,j}^{k}) - 2(\hat{f}_{i-1,j-1}^{k+1} + \hat{f}_{i-1,j+1}^{k+1} + \hat{f}_{i+1,j-1}^{k} + \hat{f}_{i+1,j+1}^{k}) - (\hat{f}_{i-2,j}^{k+1} + \hat{f}_{i,j-2}^{k+1} + \hat{f}_{i,j+2}^{k} + \hat{f}_{i+2,j}^{k})$$

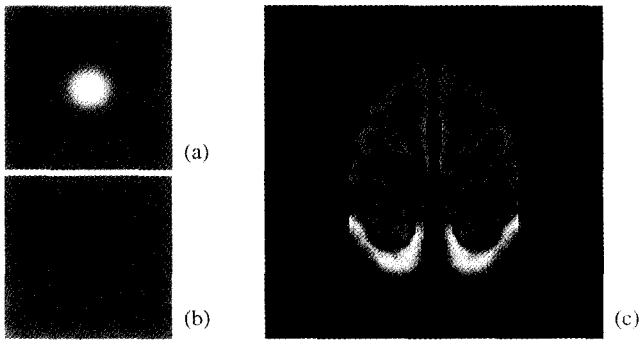

Fig. 1. Phantoms used in the simulations. (a) Phantom A. (b) Phantom B. (c) Phantom C derived from primate autoradiograph. Phantoms A and B comprise blobby hot and cold regions, respectively, which represent important regions in realistic phantom C.

for TP. Note that an ICM uses a raster-scan update in which each pixel is replaced as soon as it is updated.

Finally, we tried simple FBP reconstructions, where the incorporation of smoothing spline models is in the form of a simple linear apodization. We implemented the apodization in the Fourier domain of the projection data[14], where the angle-independent apodizing filters that multiply the ramp filter take the forms:

$$A_{MM}(\omega) = \frac{1}{1+\lambda\omega^2} \text{ and } A_{TP}(\omega) = \frac{1}{1+\lambda\omega^4}$$

for membrane and thin plate, respectively. Note that λ now assumes the role as a cutoff frequency instead of a weighting term in an energy function.

EXPERIMENTS AND RESULTS

To test the quantitative performance of reconstruction algorithms, we used the 2-D phantoms shown in Fig. 1. The mathematical phantoms A and B comprise blobby hot and cold regions with nonzero constant background. Both hot and cold regions have 25 pixel diameter, and their contrast of peaks relative to the background is 100%. Figure 1 (b) shows a 128×128 realistic[11] phantom C obtained from primate autoradiograph[16] with the benzodiazepine neuroreceptor agent Iomazenil (^{123}I). Autoradiographs provide "ground truth" functional patterns of radionuclide concentration and can be useful for designing priors in Bayesian reconstruction[16]. Further details on autoradiography can be found in[16,17]. In our experiments, we used phantoms A and B for regional quantitation, and phantom C for the overall quality of image reconstruction.

For reconstruction algorithms, we considered ML-EM, MAP-MM, MAP-TP, FBP-MM, and FBP-TP. For projection data from 64×64 and 128×128 phantoms, we used 65 projection angles over 360° with 96 detector bins and 129 projection angles over 360° with 192 detector bins, respectively. In this work, we considered attenuation effects only; each projection ray was attenuated by the constant attenuation factor of 0.15cm^{-1}. For simulations and corrections of the attenuation effects, we used a method proposed by Liang *et al.*[18] that utilizes the Siddon's method[19] to recursively compute attenuation factors along each projection ray starting at the pixel closest to the detector. At each stage of our iterative reconstructions, compensation consisted of simply an attenuated forward projection. The noise levels used in our experiments were 500K for phantoms A and C, and 464K for phantom B.

Figure 2 shows anecdotal reconstructions for phantom C. Figures 2(a) and (f) show the typical behavior of ML-EM; the results for fewer iterations are smoother than those for more iterations but incur relatively larger bias errors. Figures 2(b)(c) and (g)(h) show the MAP results for different values of λ. Note that, for MM, the bias in both high and low-activity regions increases considerably as λ increases. However, it is important to point out that the degree of oversmoothness for MAP-TP is much less than that for MAP-MM. This implies that TP is less sensitive to variations of the smoothing parameter than MM. This is also true for the FBP reconstructions in Figs. 2(d)(e) and (i)(j). Close inspection reveals that the MAP-TP reconstruction captures subtle aspects of phantom C better than other algorithms used in the simulation.

To characterize, in an ensemble sense, the effects of the hyperparameter λ for the MM and TP priors and the number of iterations for ML-EM, we first generated 50 Monte Carlo noise trials by adding independent realizations of Poisson noise to the noiseless projection data. For each set of noisy projection data, reconstructions using the MM and TP priors were performed for seven values of λ : $\lambda_i = 0.5\times2^i$, $i=0,1,2,3,4,5,6$. Thus the total number of reconstructions for each algorithm was 350. Here, the range of λ is realistic in that the λ that yields a minimum of root-mean squared error (RMSE) is near the center of the range. Since the ICM algorithm is iterative, we needed to choose a sufficient number of iterations after which the change in

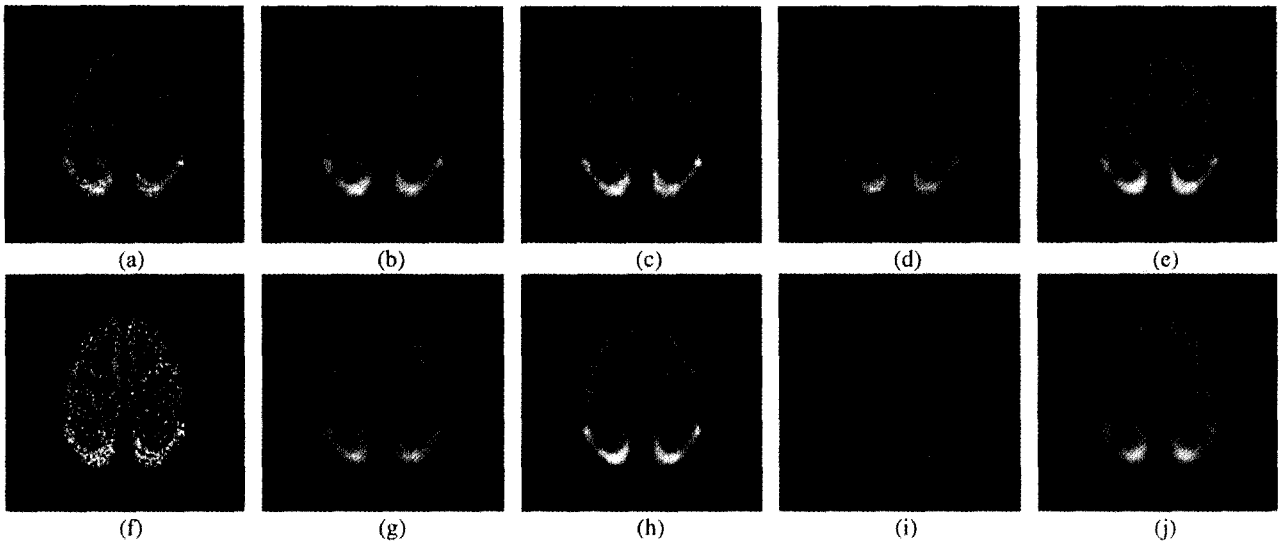

Fig. 2. Anecdotal reconstructions for phantom C. (a) ML-EM, 20 iterations (b) MAP-MM $\lambda=2$ (c) MAP-TP, $\lambda=2$ (d) FBP-MM, $\lambda=2$ (e) FBP-TP, $\lambda=2$ (f) ML-EM, 80 iterations (g) MAP-MM, $\lambda=16$ (h) MAP-TP, $\lambda=16$ (i) FBP-MM, $\lambda=16$ (j) FBP-TP, $\lambda=16$

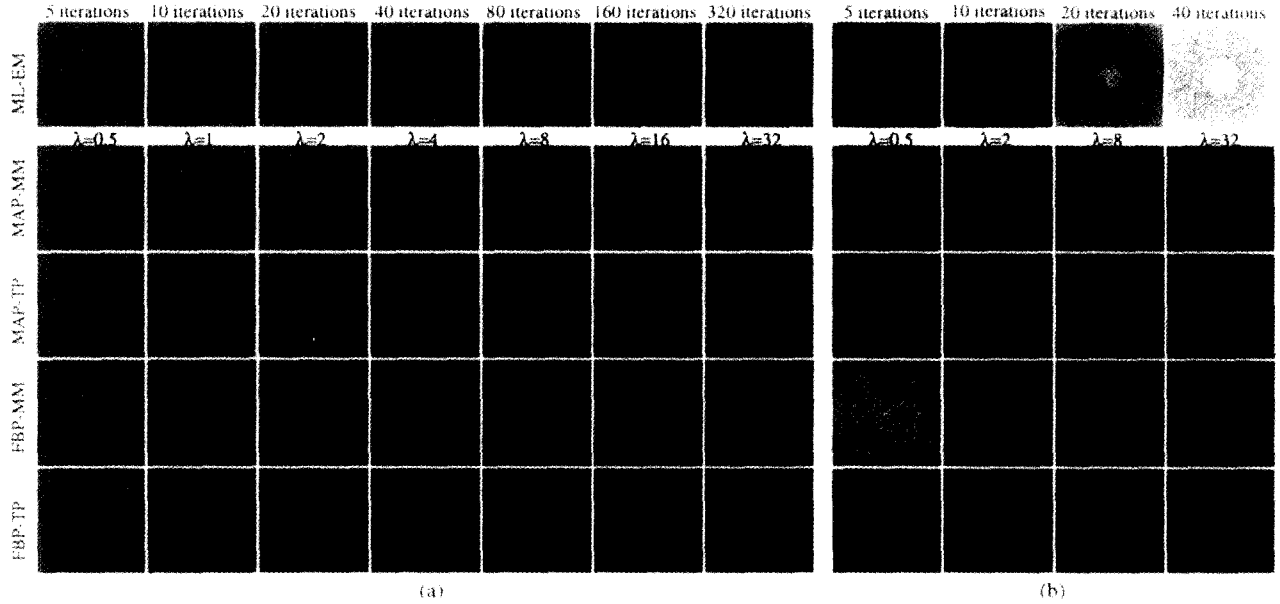

Fig. 3. Pointwise bias and STD images for phantom A. (a) Pointwise bias images. (b) Pointwise STD images

reconstruction was negligible. The number of iterations used in the experiments was 200 for both MM and TP reconstructions. (The total computation time needed to reconstruct a 64×64 image with 200 iterations was approximately 20 seconds on a SUN UltraSparc I 170 workstation.) For the ML-EM algorithm, the estimates from seven different iteration numbers, $n_i=5\times2^i$, $i=0,1,2,3,4,5,6$, were achieved for subsequent statistical analysis. (This is qualitatively equivalent to defining λ_i for TP and MM.) For FBP with MM and TP filters, we again used seven values of λ : $\lambda_i=0.5\times2^i$, $i=0,1,2,3,4,5,$. It is interesting to note that the range of λ for FBP is the same as that for MAP, and, as shown in the simulation results, this yields comparable results in regional quantitation performance to other algorithms used in the experiments.

To evaluate the reconstructions quantitatively, we computed bias and standard deviation (STD) images. A bias image, b_{ij}, is defined as $b_{ij}=\frac{1}{K}\sum_{k=1}^{K}(\hat{f}_{ij}^{k}-f_{ij})$, where $\hat{f}_{ij}^{k}$ is the kth reconstruction of phantom f at location (i,j) and

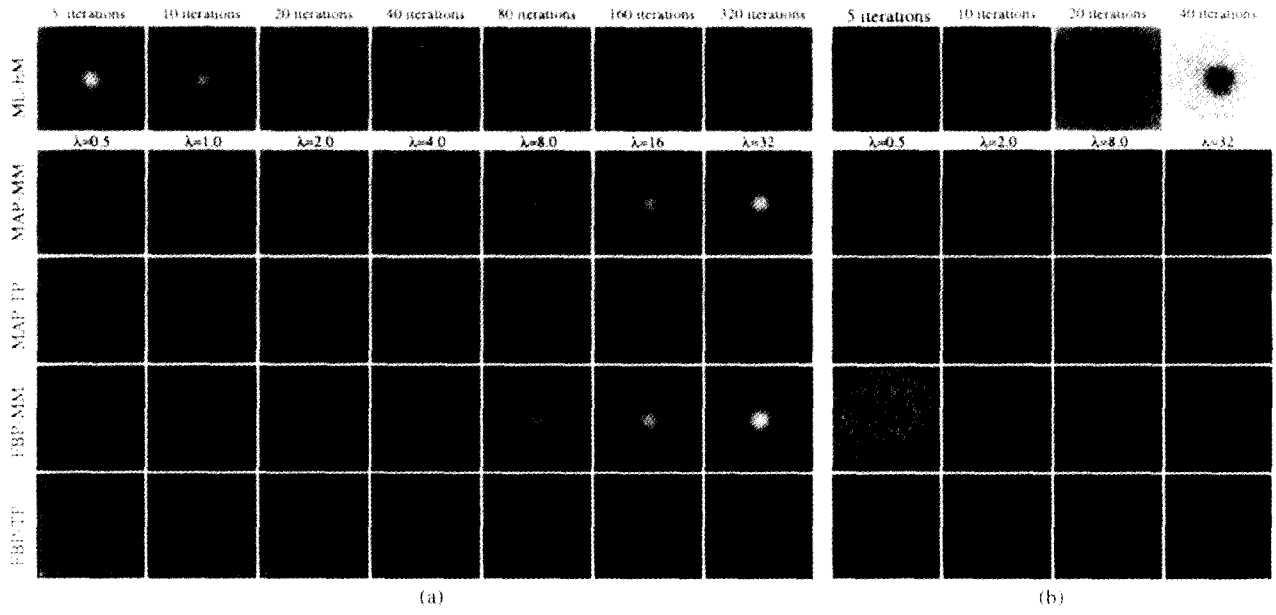

Fig. 4. Pointwise bias and STD images for phantom B. (a) Pointwise bias images. (b) Pointwise STD images

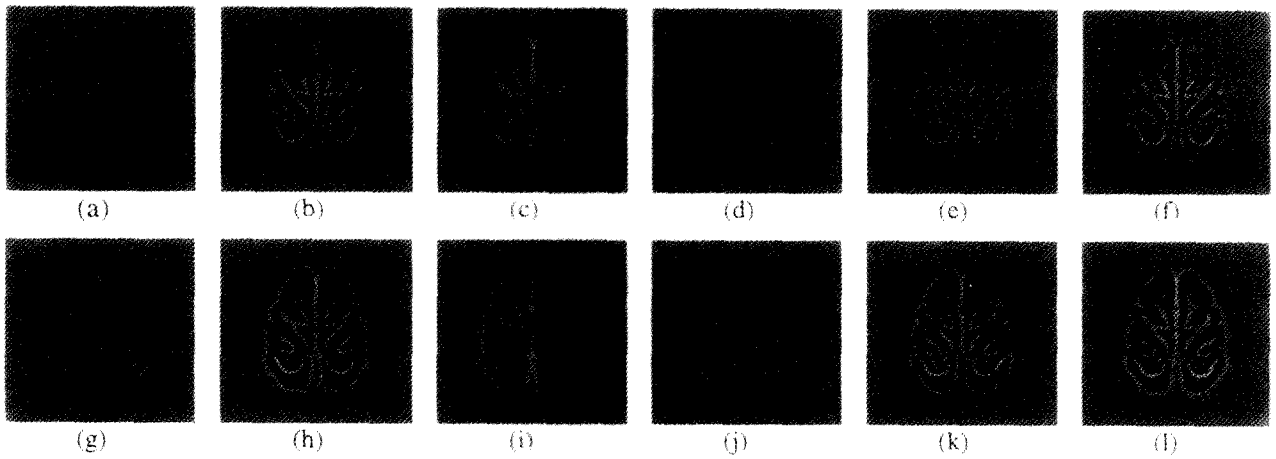

Fig. 5. Pointwise bias images for phantom C. (a) MAP-MM, λ=0.5 (b) MAP-MM λ=4 (c) MAP-MM, λ=32 (d) MAP-TP, λ=0.5 (e) MAP-TP, λ=4 (f) MAP-TP, λ=32 (g) FBP-MM, λ=0.5 (h) FBP-MM, λ=4 (i) FBP-MM, λ=32 (j) FBP-TP, λ=0.5 (k) FBP-TP, λ=4 (l) FBP-TP, λ=32

the summation is over K=50 independent noise trials. To display the bipolar bias image, an intermediate grey scale value of 128 out of 256 levels was used as zero bias. A standard deviation image, s_{ij}, is defined as

$s_{ij}=\sqrt{\frac{1}{K-1}\sum_{k=1}^{K}(\hat{f}_{ij}^{k}-\bar{f}_{ij})^2}$ where $\bar{f}_{ij}$ is the mean of $\hat{f}_{ij}$ over the noise trials defined as $\bar{f}_{ij}=\frac{1}{K}\sum_{k=1}^{K}\hat{f}_{ij}^{k}$.

Figures 3 and 4 show pointwise bias and STD images for phantoms A and B, respectively, where the same grey scale normalization is used for all to allow fair comparisons. The first row shows the usual bias/variance tradeoff inherent in ML-EM. Fewer iterations lead to lower variance but larger bias, and the opposite is true for the larger number of iterations. Note that the bias is negative in high-count regions (Fig. 3), and positive in low-count regions (Fig. 4). The second and third rows show the bias/STD images for MAP-MM and MAP-TP, respectively. Note that bias for MAP-TP is considerably less sensitive to the variations of λ than that for MAP-MM at little change in variance. The FBP results show a similar negative and positive biases in hot and cold regions, respectively, but the effect is ameliorated by the use of the TP filter. FBP algorithms "spread"

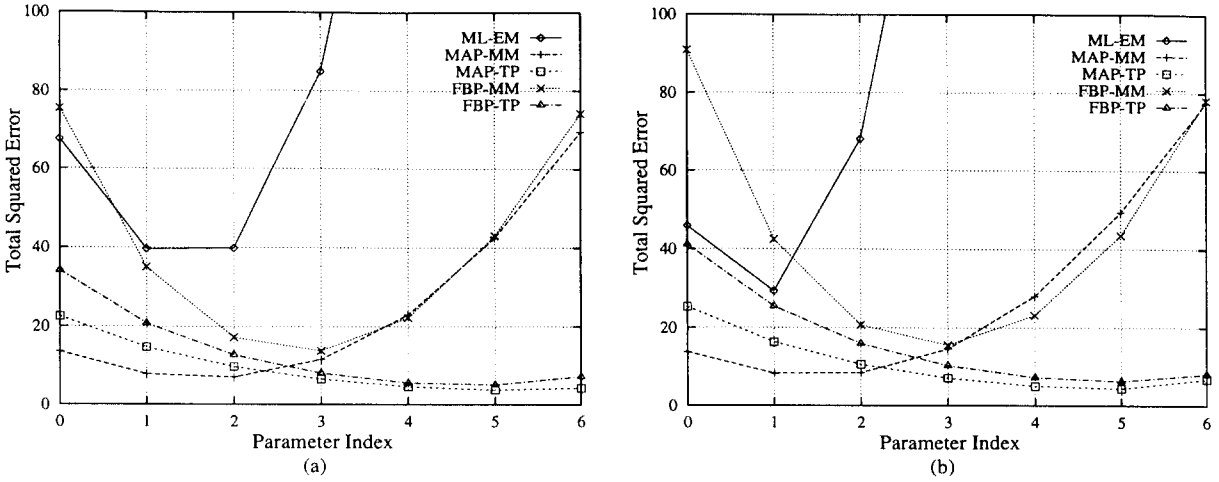

Fig. 6. Total squared error t^2. The abscissa indexes either λ_i for MAP and FBP or n_i for ML-EM. (a) Total squared error for phantom A. (b) Total squared error for phantom B.

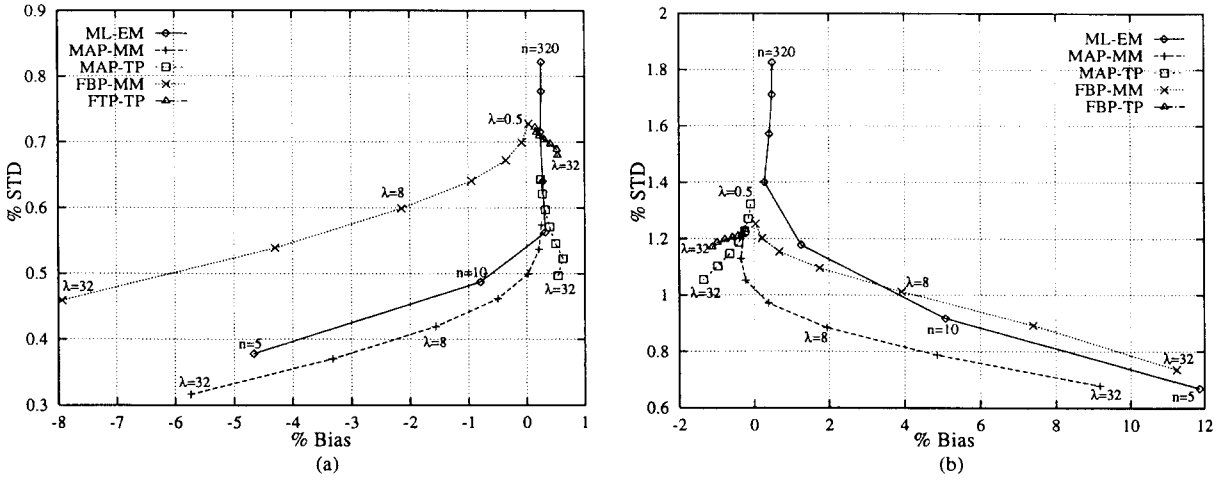

Fig. 7. The effects of several different values of smoothing parameter λ in MAP-MM, MAP-TP, FBP-MM, and FBP-TP. (a) Tradeoff between bias and STD for phantom A. (b) Tradeoff between bias and STD for phantom B.

variance across the image and, for these phantoms, the FBP-TP results actually achieve lower variance relative to MM. Figure 5 shows pointwise bias images for phantom C. As in the cases for phantoms A and B, bias for MAP-TP and FBP-TP is considerably less sensitive to the variations of λ than that for MAP-MM and FBP-MM, respectively. The results for the STD images are not reported here since their behavior is similar to the results from phantoms A and B. It is interesting to note that, for phantom C, bias for MAP-MM and MAP-TP is less sensitive to the variations of λ than that for FBP-MM and FBP-TP, respectively.

Figure 6 summarizes results in Figs. 3 and 4 in terms of total squared error t^2, computed as $t^2=\sum_{ij}(b_{ij}^2+s_{ij}^2)$. In Fig. 6 the abscissa indexes either the seven different values of smoothing parameter ($\lambda_i=0.5\times 2^i$, $i=0,1,2,\cdots,6$) or the number of iterations in ML-EM ($n_i=5\times 2^i$, $i=0,1,2,\cdots,6$). Note that both MAP-TP and FBP-TP exhibit low total squared error over the range of smoothing parameter, and the minimum of t^2 at $\lambda_5=16$ for MAP-TP is indeed smaller than that for other algorithms used in the simulation.

To assess regional quantitation performance, we also compared regional bias and variance for each given λ. This

measure is simply the bias and variance of a random variable $Z_R^k = \frac{1}{m}\sum_{ij\in R}\hat{f}_{ij}^k$, which is equal to the average count level in a region R comprised of m pixels. The appropriate regional definitions are

$$B_R = \frac{1}{K}\sum_{k=1}^{K}(Z_R^k - Z_R) \tag{5}$$

for regional bias, and

$$STD_R = \sqrt{\frac{1}{K-1}\sum_{k=1}^{K}(Z_R^k - \bar{Z}_R)^2} \tag{6}$$

for regional standard deviation, where

$$Z_R = \frac{1}{m}\sum_{ij\in R} f_{ij} \text{ and } \bar{Z}_R = \frac{1}{K}\sum_{k=1}^{K} Z_R^k$$

The percent bias and the percent STD are then the quantities $\frac{B_R}{Z_R}\times 100$ and $\frac{STD_R}{Z_R}\times 100$, respectively. To test regional quantitation performance, we selected a circle, which covers the blob region, as a region of interest (ROI) for both phantoms A and B, and evaluated regional bias and STD within the region using (5) and (6), respectively. Figures 7 (a) and (b) show %bias versus %STD curves for phantoms A and B, respectively. Note that the use of second-derivatives in MAP-TP and FBP-TP both yield excellent "robustness" in both bias and variance in that the TP leads to very low bias error over a large range of smoothing parameter, while keeping a reasonable variance. Other algorithms can exhibit smaller variance, but this is possible only at the cost of huge bias.

DISCUSSION AND CONCLUSION

We have considered the thin-plate prior which is a simple modification of the conventional membrane prior to one less sensitive to variations in first spatial derivatives. The results from the quantitative performance test show that, for comparable performance to MAP-MM in variance, MAP-TP leads to reduced bias for most of the regions studied here. In addition, MAP-TP reveals considerably less sensitivity in bias to the variations of hyperparameter than MAP-MM. This same advantage is achieved when the thin plate and membrane regularizers are implemented as an apodizing filter in an FBP algorithm. However, FBP reconstructions involve patterning artifact and are more sensitive to hyperparameters than MAP for the realistic phantom used in our experiments. For ML-EM with several different iterations, the tradeoff between bias and variance is less favorable than other algorithms considered here.

We note that, although quadratic smoothing priors may not perform as well in edge regions as nonquadratic priors, the simpler quadratic priors present an easier hyperparameter estimation problem[11,20]. Therefore, the use of TP prior would alleviate the problem of hyperparameter estimation by allowing a large range of hyperparameter as well as presenting an easier way of hyperparameter estimation.

A clinical application of the TP prior is currently under investigation; our preliminary results from practical studies show similar advantages of the TP prior as reported in this paper.

REFERENCES

1. S. Geman and D.E. McClure, *"Bayesian Image Analysis: an Application to Single Photon Emission Tomography", In Proceedings of the American Statistical Association,* 1995.
2. T. Hebert and R. Leahy, *"A Generalized EM Algorithm for 3-D Bayesian Reconstruction for Poisson Data Using Gibbs Priors", IEEE Trans. Med. Imaging,* MI-8(2), pp. 194-202, June 1989.
3. V.E. Johnson, W.H. Wong, X. Hu, and C. Chen, *"Bayesian Reconstruction of PET Images Using Gibbs Priors",* In D. A. Ortendahl and J. Lacer, editors, *Information Processing in Medical Imaging,* pp. 15-28, Wiley-Liss, 1989.
4. P.J. Green, *"Bayesian Reconstructions from Emission Tomography Data Using a Modified EM Algorithm", IEEE Trans. Med. Imaging,* MI-9(1), pp. 84-93, March 1990.
5. G. Gindi, M. Lee, A. Rangarajan, and G. Zubal, *"Bayesian Reconstruction of Functional Images Using Anatomical Information as Priors", IEEE Trans. Med. Imaging,* MI-12, pp. 670-680, Dec. 1993.
6. J.A. Fessler, *"Penalized Weighted Least-Squares Image Reconstruction for Positron Emission Tomography", IEEE Trans. Med. Imaging,* MI-13(2), pp. 290-300, June 1994.
7. S.J. Lee, A. Rangarajan, and G. Gindi, *"Bayesian Image Reconstruction in SPECT Using Higher Order Mechanical Models as Priors", IEEE Trans. Med. Imaging,* MI-14(4), pp. 669-680, Dec. 1995.
8. L. Kaufman, *"Maximum Likelihood, Least Squares, and Penalized Least Squares for PET", IEEE Trans. Med. Imaging, IEEE Trans. Med. Imaging,* MI-12(2), pp. 200-214,

June 1993.

9. V.E. Johnson, W.H. Wong, X. Hu, and C.T. Chen, *"Image Restoration Using Gibbs Priors: Boundary Modeling, Treatment of Blurring, and Selection of Hyperparameter"*, *IEEE Trans. Pattern Analysis and Machine Intelligence,* PAMI-13(5), pp. 413-425, May 1991.
10. G. Gindi, A. Rangarajan, M. Lee, P.J. Hong, and G. Zubal, *"Bayesian Reconstruction for Emission Tomography via Deterministic Annealing"*, In H. Barrett and A. Gmitro, editors, *Information Processing in Medical Imaging*, pp. 322-338, Springer-Verlag, 1993.
11. S.J. Lee, G.R. Gindi, I.G. Zubal, and A. Rangarajan, *"Using Ground-Truth Data to Design Priors in Bayesian SPECT Reconstruction"*, In Y. Bizais, C. Barillot, and R. D. Paola, editors, *Information Processing in Medical Imaging*, pp. 27-38, Kluwer Academic Publishers, 1995.
12. Z. Zhou, R.M. Leahy, and E.U. Mumcuoglu, *"Maximum Likelihood Hyperparameter Estimation for Gibbs Priors with Applications to PET"*, In Y. Bizais, C. Barillot, and R.D. Paola, editors, *Information Processing in Medical Imaging*, pp. 39-51, Kluwer Academic Publishers, 1995.
13. S. Geman and D.E. McClure, *"Statistical Methods for Tomographic Image Reconstruction"*, Bulletin of the International Statistical Institute, LII-4, pp. 5-21, 1987.
14. S.J. Lee, I.T. Hsiao, and G.R. Gindi, *"The Thin Plate as a Regularizer in Bayesian SPECT Reconstruction"*, *IEEE Trans. Nuclear Science,* NS-44(3), pp. 1381-1387, June 1997.
15. J. Besag, *"On the Statistical Analysis of Dirty Pictures"*, *Journal of the Royal Statistical Society,* Series B, 48(3), pp. 259-302, 1986.
16. J.L. Lear, *"Principles of Single and Multiple Radionuclide Autoradiography"*, In M.E. Phelps, J.C. Mazziotta, and H. R. Schelbert, editors, *Positron Emission Tomography and Autoradiography,* chapter 5, Raven Press, New York, NY, 1986.
17. L.T. Dillman and F.C. Von der Lage, *"Radionuclide Decay Schemes and Nuclear Parameters for Use in Radiation-Dose Estimation (in NM/MIRD Pamphlet No. 10)"*, Technical report, Oak Ridge National Laboratory, Oak Ridge, TN.
18. Z. Liang, T.G. Turkington, D.R. Gilland, R.J. Jaszczak, and R.E. Coleman, *"Simultaneous Compensation for Attenuation, Scatter and Detector Response for SPECT Reconstruction in Three Dimensions"*, Phys. Med. Biol., 37, pp. 587-603, 1991.
19. R. Siddon, *"Fast Calculation of the Exact Radiological Path for 3D CT Array"*, Med. Phys., 12, pp. 252-255, 1985.
20. Z. Zhou and R. Leahy, *"Approximate Maximum Likelihood Parameter Estimation for Gibbs Priors"*, Technical Report TR-285, Signal and Image Processing Institute, University of Southern California, June 1995.